JGR Atmospheres

RESEARCH ARTICLE
10.1029/2025JD043487

On the Potential Role of Lubrication Oil Particles in Contrail Formation for Kerosene and Hydrogen Combustion

Josef Zink[1], **Simon Unterstrasser**[1], **and Tina Jurkat-Witschas**[1]

[1]Deutsches Zentrum für Luft- und Raumfahrt, Institut für Physik der Atmosphäre, Oberpfaffenhofen, Germany

Key Points:

- Particles originating from lubrication oil may serve as nuclei for the formation of contrail ice crystals
- Oil particles could be the dominant nuclei when soot particle numbers are low (soot-poor regime) or zero (e.g., for hydrogen combustion)
- Measurements are needed to constrain our hypothetical simulation scenarios

Correspondence to:
J. Zink,
josef.zink@dlr.de

Citation:
Zink, J., Unterstrasser, S., & Jurkat-Witschas, T. (2025). On the potential role of lubrication oil particles in contrail formation for kerosene and hydrogen combustion. *Journal of Geophysical Research: Atmospheres*, *130*, e2025JD043487. https://doi.org/10.1029/2025JD043487

Received 24 JAN 2025
Accepted 8 JUN 2025

Author Contributions:
Conceptualization: Josef Zink, Simon Unterstrasser, Tina Jurkat-Witschas
Data curation: Josef Zink
Formal analysis: Josef Zink
Funding acquisition: Simon Unterstrasser, Tina Jurkat-Witschas
Investigation: Josef Zink
Methodology: Josef Zink, Simon Unterstrasser
Project administration: Simon Unterstrasser
Software: Josef Zink, Simon Unterstrasser
Supervision: Simon Unterstrasser
Validation: Josef Zink
Visualization: Josef Zink
Writing – original draft: Josef Zink
Writing – review & editing: Josef Zink, Simon Unterstrasser, Tina Jurkat-Witschas

Abstract The radiative forcing caused by contrail cirrus is nonlinearly influenced by the number of ice crystals formed in the exhaust plume behind an aircraft engine. This ice crystal number strongly depends on the properties (number, size, and solubility) of condensation nuclei in the plume available for droplet activation with subsequent freezing. In this ice crystal formation process, the relative importance of plume particles originating from lubrication oil is unclear. Therefore, we have extended the particle-based Lagrangian Cloud Module in the box model approach to simulate the formation of ice crystals on such oil particles. With this extended box model, we performed simulations for many different scenarios of emitted oil particle numbers and sizes. We examine the activation of these oil particles and investigate their competition with soot for kerosene combustion and with ambient aerosols for hydrogen combustion. Furthermore, we study the relative importance among weakly soluble/insoluble oil particles and well-soluble volatile particles from the combustion process. For present-day soot emissions, the number of ice crystals formed on oil particles may be masked by those formed on soot. However, these oil particles may be abundant enough to dominate ice crystal formation in soot-poor or hydrogen combustion scenarios. This may occur when a small amount of lubrication oil (on the order of a few milliliters per hour) evaporates in the hot exhaust plume and nucleates new particles with a size of a few nanometers during the subsequent plume cooling.

Plain Language Summary Contrail cirrus clouds contribute significantly to the overall climate impact of aviation. These cirrus clouds develop from linear contrails formed by an aircraft engine under certain atmospheric conditions. The climate impact is the stronger the more ice crystals the young contrails contain. For conventional kerosene combustion, these ice crystals primarily form on the emitted soot particles. However, when the number of soot particles is reduced or is zero (e.g., for hydrogen combustion), other particles in the exhaust plume become important. One possible source of such particles is lubrication oil. In this study, we investigate the potential role of such oil particles in the contrail formation process. We examine their activation behavior and their relative importance compared to other ice-forming particles. The results suggest that these oil particles may contribute significantly to the total ice crystal number in soot-poor or hydrogen combustion scenarios. As many different scenarios are investigated in our study, it is essential to measure their actual impact in in situ flight campaigns. Nevertheless, our study clearly demonstrates that on the way to aviation technologies with reduced climate impact, every effort should be made to keep the number of oil particles in aircraft exhausts low.

1. Introduction

As part of the aviation non-CO_2 effects, contrail cirrus constitute a significant contributor to the total effective radiative forcing of aviation (Kärcher, 2018; Lee et al., 2021). The optical properties and life cycle of contrail cirrus and thus the climate impact strongly depend on the number of contrail ice crystals formed (e.g., Burkhardt et al., 2018; Unterstrasser & Gierens, 2010). These ice crystals form primarily on emitted soot particles for conventional passenger aircraft engines (e.g., Kärcher & Yu, 2009; Kleine et al., 2018). Because of the strong nonlinear relation between the global contrail cirrus radiative forcing and the number of contrail ice crystals formed (Bier & Burkhardt, 2022; Burkhardt et al., 2018), only a strong reduction in soot number and other particles is expected to have a substantial climate benefit.

Blending conventional Jet-A1 fuel with sustainable aviation fuels (SAF) reduces the soot particle number attributed to the lower aromatic content of SAF (Bräuer et al., 2021; Moore et al., 2017; Voigt et al., 2021). This can reduce young-contrail ice crystal number by up to 70% depending on the SAF proportion (Voigt et al., 2021). Moreover, using a 100% SAF fuel, Märkl et al. (2024) measured a reduction of 35% in soot number and a

reduction of 56% in ice crystal number. They attributed the stronger reduction in ice crystals compared to the soot reduction with a low sulfur content leading to a reduced ice activation of the soot particles. Similarly, hydroprocessing can reduce the aromatic content of conventional kerosene (Quante et al., 2024), offering another pathway to lower soot emissions and contrail ice crystal formation.

Soot-free exhaust air is expected from hydrogen combustion due to the absence of carbon compounds in the fuel used. The usage of hydrogen in aviation, either via direct combustion or in a fuel-cell system (Richardson, 2025), is a potential pathway for the decarbonization of the aviation sector. Previous investigations on contrails from hydrogen-powered aircraft were rather academically driven (Grewe et al., 2017), whereas today, the goal of commercial hydrogen-powered aircraft is set from industry (Airbus, 2020) and politics. For thermodynamic reasons, contrails from hydrogen combustion can form at higher temperatures according to the Schmidt-Appleman threshold criterion and exhibit higher supersaturations due to a relative increase of the energy-specific water vapor emission index by a factor of around 2.6 (Bier et al., 2024; Schumann, 1996). Recently, Bier et al. (2024) studied contrail formation in such hydrogen exhaust plumes. They assumed that no exhaust particles that serve as condensation nuclei are emitted and liquid droplet activation and ice crystal formation occurs only on entrained ambient aerosols. Their simulation results suggest that the ice crystal number in the early phase is typically reduced by more than 80%–90% compared to conventional contrails.

However, Kärcher and Yu (2009) showed for kerosene combustion that nanometer sized ultrafine aqueous particles may activate at high supersaturations. Depending on the number of these volatile particles, the ice crystal number in the soot-poor regime may be similarly high at low temperatures as in a soot-rich regime. For conventional kerosene combustion, these volatile ultrafine particles form mainly on emitted charged molecular clusters (chemi-ions) which grow due to the condensation of water vapor, sulfuric acid, nitric acid, and unburned hydrocarbons (F. Yu & Turco, 1997). Because of the absence of sulfur and organic compounds in the hydrogen combustion process, nitrogen oxide species might be the only emitted source for the nucleation of ultrafine volatile particles there. Nitrate ions are potential precursors of ion clusters which may grow through condensation and recombination. However, their nucleation ability to form clusters of a significant size in the nanometer range has not yet been experimentally shown.

Yet, another potential non-combustion source for such volatile particles is lubrication oil. Lubrication oil is used to cool, seal and reduce friction of movable parts such as the drive shaft. Oil systems are generally sealed recirculation systems (Linke-Diesinger, 2010). Breather vents regulate the oil pressure system. This venting results in a controlled emission and releases a mist of oil. Next to the controlled oil emission, worn seals provide an additional uncontrolled sink of oil (Z. Yu et al., 2010). This uncontrolled loss is expected to be a few percent of the controlled oil emission and may vary over time with the degradation of seals, thus with aging of the engine. A typical engine lubrication oil consumption is on the order of a few hundreds of milliliters per hour (Decker et al., 2024; Linke-Diesinger, 2010). This oil consumption may vary among different engine types and thrust settings (Decker et al., 2024).

Several ground-based measurements behind dedicated engines as well as in the vicinity of airports have identified lubrication oil as a major component of aviation-induced ultrafine particulate matter (Fushimi et al., 2019; Ungeheuer et al., 2021; Z. Yu et al., 2019). Motivated by their findings from measurements at Frankfurt Airport (Ungeheuer et al., 2021), Ungeheuer et al. (2022) demonstrated in a laboratory experiment that heating oil particles to 300°C leads to the formation of a small-sized particle distribution. This occurs as the particles evaporate with subsequent nucleation and recondensation of low-volatility products. This experiment resembles conditions when lubrication oil is entrained into hot exhaust plumes, for example, through central venting systems. In another laboratory experiment, Ponsonby et al. (2024) generated oil particles and demonstrated their activation into water droplets and freezing into ice crystals. These particles generated in the laboratory were neither affected by any combustion process nor formed through nucleation and condensation of additional combustion products. They found that these oil particles behave such as insoluble but wettable particles. So far, in-flight emission measurements at cruise altitude have not been able to provide evidence of a dominant contribution of lubrication oil for the formation of nucleation mode ultrafine particles.

Although the experiment by Ponsonby et al. (2024) demonstrated that oil particles are capable of acting as condensation nuclei, their activation behavior under contrail formation conditions and their competition with other plume particles for the available water vapor are still unexplored. In this study, we examine these open points for a range of potential scenarios. We consider different levels of oil emissions and oil particle sizes

(Section 2). In a first step, we investigate the activation behavior of oil particles (Section 3.1). We then analyze their competition with other plume particles and investigate under which scenarios they can lead to a non-negligible or even dominant contribution to the total ice crystal number (Sections 3.2 and 3.3). The implications of the results are discussed in Section 4.

2. Methods

The following section briefly describes the model used in this study. It also outlines the initial conditions and our underlying assumptions.

2.1. Number of Oil Particles

We assume that part of the emitted oil is entrained into the hot plume, where it evaporates and re-nucleates. We assume that this nucleation is completed well before contrail formation starts so that we can prescribe a fixed number of emitted particles. This is justified by the fact that temperatures at which jet oil esters reach gas-phase supersaturation are typically well above 0°C (see, e.g., Figure 3 in Ungeheuer et al., 2022), whereas contrail formation starts well below 0°C. For simplicity and lack of density measurements, we assume that the re-nucleated oil particles have the same density as the original lubrication oil particles and are log-normally distributed with a geometric mean radius $\bar{r}_{\mathrm{d,oil}}$ and geometric width σ_{oil} (The probability density function of a log-normal distribution reads $n(r) = \frac{N}{\sqrt{2\pi}} \frac{1}{\ln \sigma} \frac{1}{r} \exp\left[-\frac{1}{2}\left(\frac{\ln r/\bar{r}}{\ln \sigma}\right)^2\right]$ with total number N, geometric mean radius $\bar{r}$ and geometric width σ). The number of oil particles per meter of flight path can be calculated via

$$N_{\mathrm{oil}} = \frac{\dot{V}_{\mathrm{oil,eff}}}{\frac{4}{3}\pi \bar{r}_{\mathrm{d,oil}}^3 \exp\left(\frac{9}{2}(\ln \sigma_{\mathrm{oil}})^2\right)} \frac{1}{U_\infty}, \tag{1}$$

with the aircraft speed U_∞ (=250 m s^{-1} in our case) and the effective oil emission rate

$$\dot{V}_{\mathrm{oil,eff}} = \dot{V}_{\mathrm{oil}} \cdot \alpha_{\mathrm{entrain}} \cdot \alpha_{\mathrm{evaporate}} \cdot \alpha_{\mathrm{renucleate}} \cdot \alpha_{\mathrm{scavenging}} \cdot \beta_{\mathrm{condensates}} \ . \tag{2}$$

Here, $\dot{V}_{\mathrm{oil}}$ is the oil emission/loss (in units "volume per time") from the venting system to the environment. The different α-values, which are supposed to range from zero to one, account for different physical effects: $\alpha_{\mathrm{entrain}}$ represents the fraction of the emitted oil entrained into the hot exhaust plume. This value may largely depend on the position of the venting system relative to the engine. $\alpha_{\mathrm{evaporate}}$ is the fraction of entrained oil that evaporates. We assume that the fraction $1 - \alpha_{\mathrm{evaporate}}$ consists of larger particles originating from oil entrained when the plume is already cooled down so that the oil particles do not evaporate. We assume that the volume fraction $1 - \alpha_{\mathrm{evaporate}}$ of the large particles does not significantly contribute to the overall number. $\alpha_{\mathrm{renucleate}}$ is the fraction of evaporated oil that forms new particles. The fraction $1 - \alpha_{\mathrm{renucleate}}$ remains either in the gas phase or condenses on other particles such as soot or the larger oil particles that did not evaporate. $\alpha_{\mathrm{scavenging}}$ is the fraction of the newly formed particles that is not scavenged by other plume particles. $\beta_{\mathrm{condensates}}$ is assumed to be larger than or equal to one and accounts for condensates of other combustion products on the re-nucleated oil particles. Equation 2 should be interpreted as conceptual framework that illustrates different physical effects that may reduce the total volume and mass of the oil particles. The values of the different efficiencies α_x are currently largely unquantified and can depend on engine and fuel characteristics (see also Section 4). Even though, the total effective volume of the lubrication oil particles serving as ice crystal precursors might be much smaller than the volume of oil lost in first place, the number of oil particles can be higher than initially due to their smaller size. Note that for a prescribed N_{oil} value, $\dot{V}_{\mathrm{oil,eff}}$ can differ by several orders of magnitude, depending on the prescribed values of $\bar{r}_{\mathrm{d,oil}}$ and σ_{oil} (Equation 1 and Figure 1).

2.2. Box Model Setup

We perform simulations with the Lagrangian Cloud Module (LCM), first described in Sölch and Kärcher (2010) and typically employed in a version fully coupled with the large-eddy simulation (LES) model EULAG to simulate pure ice clouds. Unlike Eulerian cloud microphysics models, LCM employs a particle-based approach and ice crystals are represented by simulation particles (SIPs). For the present study, a box model version of LCM

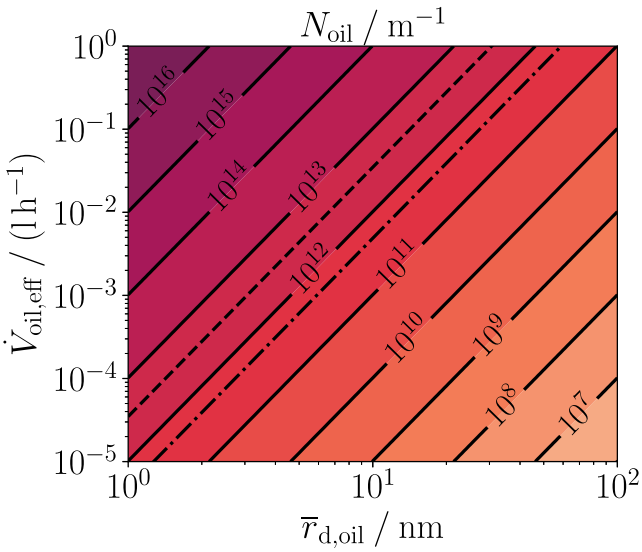

Figure 1. Number of oil particles per meter of flight path N_{oil} as a function of geometric mean radius $\bar{r}_{d,oil}$ and effective oil emission $\dot{V}_{oil,eff}$ according to Equation 1 with $\sigma_{oil} = 1.6$ (solid contour lines). The contour line of $N_{oil} = 10^{12}$ m^{-1} is also shown for $\sigma_{oil} = 2.02$ (dashed) and $\sigma_{oil} = 1.27$ (dash-dotted). The relative distances between the solid, dashed, and dash-dotted lines would be the same for each N_{oil} value.

is employed, which is not coupled to EULAG. This LCM variant has been extended recently to capture the microphysics of contrail formation (via the liquid phase). A full description of the LCM box model is given in Bier et al. (2022, 2024), which simulate contrail formation on soot for kerosene combustion and on ambient aerosol for hydrogen combustion, respectively. As in Bier et al. (2024), we prescribe the plume dilution along an ensemble of 1,000 different trajectories to account for the plume cooling and heterogeneity. These are suitably merged trajectories from a data set of 25,000 trajectories sampling a single aircraft exhaust plume behind an engine of an A340-300 aircraft as simulated by a 3D large-eddy simulation (Vancassel et al., 2014). Each trajectory represents a fraction of plume volume and plume air mass and we apply the box model separately for each trajectory. The results from the 1,000 (sub-)simulations are then suitably combined: for extensive quantities (e.g., ice crystal number), we present the sum over all 1,000 trajectories and for intensive quantities (e.g., temperature) we present a mass-weighted average over the trajectory ensemble (see Supplement in Bier et al., 2022).

Engine and fuel properties (water vapor emission index EI_v, specific heat of combustion Q, overall propulsion efficiency η and fuel consumption m_C) and engine exit conditions (exit temperature T_E and exit area A_E) are set as in Bier et al. (2024) and summarized in Table 1. Ambient temperature T_a is a crucial parameter for contrail formation and simulations are performed and analyzed for several T_a values. Ambient pressure p_a and relative humidity over ice

Table 1
Simulation Setup

Kerosene fuel and engine properties:	$EI_v = 1.26$ kg kg^{-1}, $Q = 43 \cdot 10^6$ J kg^{-1}
	$\eta = 0.36$, $m_C \approx 3.1$ g m^{-1}[a]
Hydrogen fuel and engine properties:	$EI_v = 8.94$ kg kg^{-1}, $Q = 120 \cdot 10^6$ J kg^{-1}
	$\eta = 0.36$, $m_C \approx 1.1$ g m^{-1}[a]
Engine exit conditions:	$T_E = 580$ K, $A_E = 0.25\pi$ m^2
Ambient conditions:	$T_a = [215, 220, 225, 232]$ K, $p_a = 260$ hPa, $RH_{ice,a} = 120\%$
Soot properties:	$\bar{r}_{d,s} = 15$ nm, $\sigma_s = 1.6$, $\kappa_s = 0.005$
	$EI_s = [10^{12}, 10^{13}, 10^{14}, 10^{15}, 10^{16}]$ kg^{-1}
	corresponds to:[b]
	$N_s \approx 3.1 \cdot [10^9, 10^{10}, 10^{11}, 10^{12}, 10^{13}]$ m^{-1}
Ambient aerosol properties:	$\bar{r}_{d,aer} = 15$ nm, $\sigma_{aer} = 1.6$, $\kappa_{aer} = 0.5$
	$n_{aer} = [10^0, 10^1, 10^2, 10^3, 10^4]$ cm^{-3}
Oil particle properties:	$\bar{r}_{d,oil} = [1, 5, 15, 25]$ nm, $\sigma_{oil} = [1.27, 1.6, 2.02]$, $\kappa_{oil} = 0$
	$N_{oil} = [10^8, 10^9, 10^{10}, 10^{11}, 10^{12}, 10^{13}, 10^{14}, 10^{15}, 10^{16}]$ m^{-1}
	Corresponds to:[b]
	$EI_{oil,kerosene} \approx 3.2 \cdot [10^{10}, 10^{11}, 10^{12}, 10^{13}, 10^{14}, 10^{15}, 10^{16}, 10^{17}, 10^{18}]$ kg^{-1}
	$EI_{oil,hydrogen} \approx 9.0 \cdot [10^{10}, 10^{11}, 10^{12}, 10^{13}, 10^{14}, 10^{15}, 10^{16}, 10^{17}, 10^{18}]$ kg^{-1}
Volatile particle properties:	$\bar{r}_{d,vol} = 1$ nm, $\sigma_{vol} = 1.6$, $\kappa_{vol} = 0.5$
	$EI_{vol,kerosene} = [10^{12}, 10^{14}, 10^{15}, 10^{16}, 10^{17}]$ kg^{-1}
	$EI_{vol,hydrogen} = 2.8 \cdot [10^{12}, 10^{14}, 10^{15}, 10^{16}, 10^{17}]$ kg^{-1}
	Corresponds to:[b]
	$N_{vol} \approx 3.1 \cdot [10^9, 10^{11}, 10^{12}, 10^{13}, 10^{14}]$ m^{-1}

Note. See text for descriptions of parameter names. [a]Calculated with Eq. (4) and Eq. (10) in Bier et al. (2024) for $T_a = 225$ K. [b]Calculated with $N_x = EI_x \cdot m_C$ where x denotes the emitted particle type.

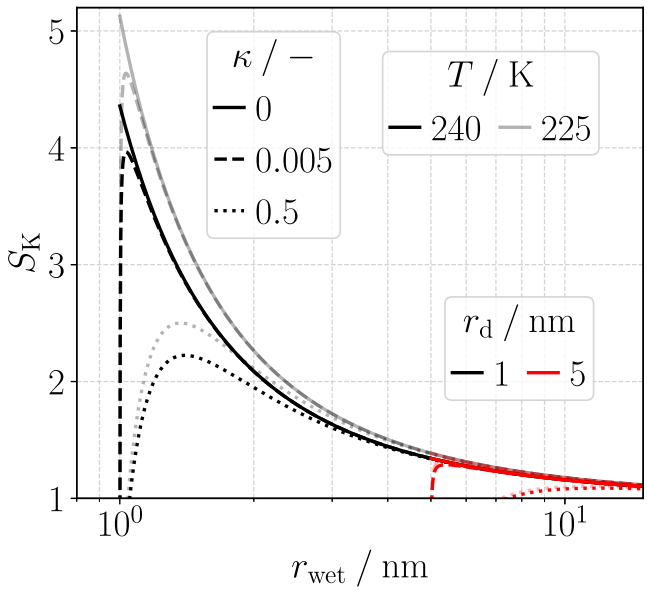

Figure 2. Equilibrium saturation ratio S_K over a droplet with wet radius r_{wet} according to κ-Köhler theory for different hygroscopicities κ (line style), two plume temperatures T (transparency), and dry radii r_d (color).

$RH_{ice,a}$, on the other hand, do not significantly affect the results and interpretations and are thus kept constant throughout the simulations shown in this study.

We consider four different particle types: soot (for kerosene combustion), ambient aerosols (for hydrogen combustion), oil particles (for both hydrogen and kerosene combustion), and volatile particles originating from the combustion products (for both hydrogen and kerosene combustion). For any particle type, we assume spherical shape and a log-normal size distribution at initialization. We use the algorithm in Unterstrasser and Sölch (2014) to generate a SIP ensemble for given size distribution properties. Typically, only a selection of particle types is switched on in a particular simulation.

For soot and ambient aerosols, we assume the baseline values for geometric mean radius $\bar{r}_d$, geometric width σ and hygroscopicity κ of Bier et al. (2022, 2024). Focusing on the oil particles, these properties are held constant throughout the simulations. The parametrizations for the activation into water droplets, their diffusional growth and freezing into ice crystals are described in detail in Bier et al. (2022) for soot and in Bier et al. (2024) for ambient aerosols. We prescribe a wide range of soot number emission indices EI_s, including present-day values as well as soot-poor scenarios accounting for technological progress in reducing the soot number. For $EI_s = 10^{15}$ kg^{-1}, the corresponding soot number per meter of flight path for the given fuel consumption is $N_s \approx 3.1 \cdot 10^{12}$ m^{-1} (Table 1). Following Equation 1, this corresponds to a soot volume emission rate $\dot{V}_s \approx 0.1$ l h^{-1}. In addition, a wide range of ambient aerosol concentrations n_{aer} accounts for the large variability in the atmosphere (e.g., Brock et al., 2021; Kaiser et al., 2019; Minikin et al., 2003), including also a rather extreme upper value.

Based on the findings by Ponsonby et al. (2024), we treat oil particles as insoluble ($\kappa_{oil} = 0$) but wettable particles. For $\kappa = 0$, the κ-Köhler equation for calculating the equilibrium saturation over a droplet (Petters & Kreidenweis, 2007) reduces to the Kelvin term (Figure 2). We calculate this Kelvin term for the particle dry radius and assume that the oil particle take up water vapor once the plume relative humidity exceeds this critical barrier. Assuming insolubility, we use the parametrization for pure water to determine the homogeneous freezing temperatures (Bier et al., 2022; Kärcher et al., 2015; Riechers et al., 2013). We vary the geometric mean dry radius $\bar{r}_{d,oil}$ and the geometric width σ_{oil} of the log-normal distribution. The geometric width is varied so that the width of the corresponding mass distribution is halved and doubled (assuming spherical particles). The number of emitted oil particles N_{oil} (Table 1) is varied over a very large range to account for the physical considerations presented in Section 2.1. All trajectories are initialized with the same fraction of oil particles (implying a homogeneous spatial distribution of oil particles in the initial plume). This generic treatment neglects differences that result from the specific location of the venting system.

The effect of particle dry radius, hygroscopicity, and plume temperature on the critical saturation ratio (maximum of $\kappa -$ Köhler curve) is depicted in Figure 2. For a hygroscopicity $\kappa = 0$ and a dry radius $r_d = 5$ nm the Kelvin barrier for a given plume temperature is around 70% lower than for a dry radius $r_d = 1$ nm. We emphasize, that the hygroscopicity of the oil particles may be larger than zero in the kerosene combustion case due to condensation of hygroscopic compounds such as sulfuric acid (Ungeheuer et al., 2022). In contrast, the composition of hydrogen combustion emission products is largely unknown. Nitric acid is formed from oxidation of nitrogen oxides in the hydrogen combustion case. Because of its hydrophilic nature after condensation, it is expected to change the hygroscopicity of the oil particles to values larger than zero, yet it is likely lower than in the kerosene case. The amount of nitric acid formed and its ability to form particles in the exhaust plume is yet still unknown. The change of critical saturation due to a higher hygroscopicity (e.g., from zero to 0.005) for a given dry radius and plume temperature, however, is less than 10%. We therefore conclude that compared to the strong increase of the Kelvin barrier with decreasing particle dry radius, hygroscopicity has a second order effect on the nucleation ability of the oil particles. As we here prescribe a lower limit of zero, the nucleation ability and thus the number of ice crystals formed on our simulated oil particles represent a lower limit.

As outlined in Section 1, some kerosene combustion products are an additional source for the formation of volatile particles. We therefore consider two types of volatile particle modes. The first mode is the already described weakly soluble/insoluble particle mode that mainly consists of lubrication oil constituents. We characterize this mode by assigning a limiting value $\kappa_{oil} = 0$, neglecting the impact of condensates from combustion products on the hygroscopicity. In addition, we consider a well-soluble mode primarily consisting of hydrophilic combustion products, which is characterized by a considerably higher hygroscopicity (here, $\kappa_{vol} = 0.5$ is assumed). This higher hygroscopicity reduces the Kelvin barrier substantially (Figure 2). Emission indices EI_{vol} of the latter mode can be on the order of 10^{16}–10^{17} kg^{-1} (F. Yu & Turco, 1997; Haverkamp et al., 2004). We assume that the formation of the volatile particles is completed well before the onset of contrail formation. Accordingly, a fixed emission index is assumed and the volatile particles are initialized at the start of the simulation. In this study, we prescribe a range of emission indices accounting for different fuel compositions and engine settings. Since the focus is on the oil particles, we fix other properties ($\bar{r}_{d,vol}$, σ_{vol}). Although the composition of hydrogen combustion products is poorly understood, we still include an additional well-soluble volatile particle mode in our simulations. To maintain consistency, we prescribe the same number and properties of these particles as in the kerosene case, despite the likelihood of substantial differences between the two fuel types. This approach allows us to explore a range of potential scenarios under idealized conditions.

In the presentation of the results, we use different metrics for the different particle types. Following the standard of aviation community, we prescribe emission indices per kilogram of fuel burned for particles the number of which is related to the fuel consumption, such as soot and volatile particles from combustion products. In contrast, entrained ambient aerosols cannot be directly linked to the fuel consumption, so we prescribe their background number concentration. Analogously, the lubrication system is a separate system, and the emitted oil particle number is not necessarily related to the fuel consumption. Therefore, we prescribe their number per meter of flight path. Moreover, for the same total number of emitted oil particles per meter of flight path, the corresponding emission indices for hydrogen and kerosene combustion differ due to different fuel consumptions, which arise from their different combustion heats (Table 1). This complicates direct comparisons if emission indices were used. In our presentation, we consistently prescribe the total number of emitted particles per meter of flight path across the two fuel types. To help the reader and facilitate comparisons with measurements, we nevertheless provide the corresponding emission indices based on the given fuel consumptions (Table 1). While the given fuel consumptions determine the total number of emitted soot and volatile particles, the prescribed emission indices span a broad range. This variation captures a variety of engine types and operations.

3. Results

3.1. Activation of Oil Particles

First, we examine the activation of oil particles without incorporating further particle types into our simulations (Figure 3). Although these scenarios are inherently hypothetical and are unlikely to occur in reality, they are useful for understanding and interpreting the results when two or three particle types are included.

When examining the evolution of plume relative humidity in the absence of microphysics, where the evolution is solely determined by dilution, the peak supersaturations reached in the hydrogen cases are higher than those in the kerosene cases (transparent solid and dotted red curves in Figure 3a). This is because of the higher energy-specific water vapor emission index. The evolution of plume relative humidity changes substantially when microphysics is switched on and activated droplets (number N_{drop}) and ice crystals (number N_{ice}) deplete the water vapor (compare transparent and opaque red curves in Figure 3a). The activation and freezing fraction are given by

$$\phi_{act}(t) = \frac{N_{drop}(t) + N_{ice}(t)}{N_{oil}} \tag{3}$$

and

$$\phi_{frz}(t) = \frac{N_{ice}(t)}{N_{oil}}\ , \tag{4}$$

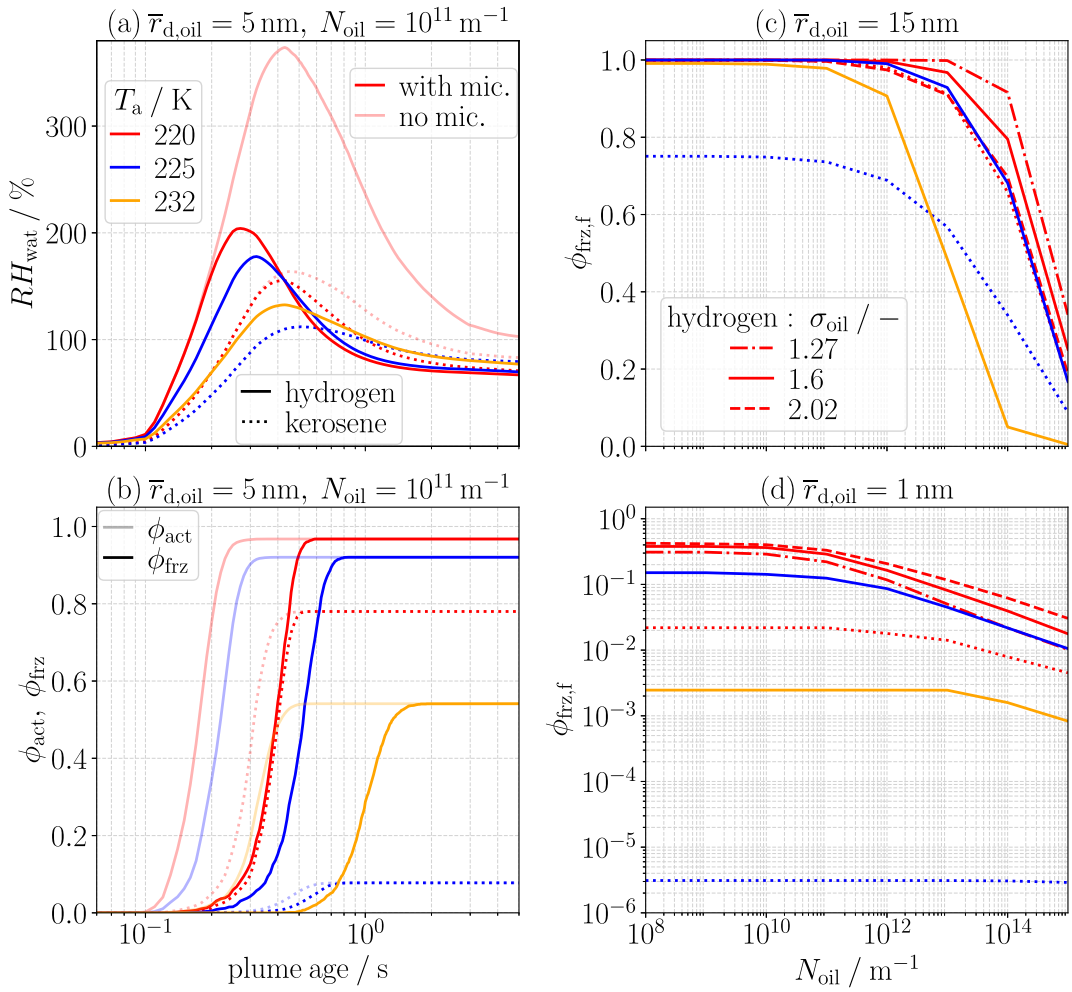

Figure 3. Activation of oil particles in kerosene and hydrogen combustion exhaust plumes without a second particle type. (a) Time evolution of plume relative humidity over water RH_{wat} for different ambient temperatures T_{a} (different colors) for hydrogen (solid) and kerosene (dotted) combustion. For $T_{\mathrm{a}} = 220$ K the time evolution without microphysics (transparent) is shown additionally. (b) Exemplary time evolution of activation fraction ϕ_{act} (transparent) and freezing fraction ϕ_{frz} (opaque) for different T_{a} (different colors) for hydrogen (solid) and kerosene (dotted) combustion. (c) Final freezing fraction $\phi_{\mathrm{frz,f}}$ as a function of oil particle number N_{oil} for a geometric mean radius $\bar{r}_{\mathrm{d,oil}} = 15$ nm. For $T_{\mathrm{a}} = 220$ K and hydrogen combustion, the geometric width is varied (different line styles; the dotted line corresponds to kerosene combustion with $\sigma_{\mathrm{oil}} = 1.6$). (d) Same as (c) but for $\bar{r}_{\mathrm{d,oil}} = 1$ nm and a logarithmic scaling of the y-axis.

respectively. Both quantities increase over time and attain larger values for lower ambient temperature (Figure 3b) as the peak plume supersaturation is higher (Figure 3a). The simulation examples depicted in the left column of Figure 3 use $\bar{r}_{\mathrm{d,oil}} = 5$ nm, $\sigma_{\mathrm{oil}} = 1.6$, and $N_{\mathrm{oil}} = 10^{11}$ m^{-1}. The higher supersaturation encountered in the hydrogen case results in an earlier activation of oil particles into water droplets. Furthermore, a larger fraction of the small particles within the size distribution are able to overcome the Kelvin barrier and activate into droplets. Consequently, the activation and freezing fraction is larger for the hydrogen case than for the kerosene case. Additionally, droplets and ice crystals can form in the hydrogen case (orange curve in Figure 3b) at temperatures where ice crystals do not form in the kerosene case in agreement with the Schmidt-Appleman criterion.

For a geometric mean radius $\bar{r}_{\mathrm{d,oil}} = 15$ nm (almost) all emitted oil particles freeze into ice crystals for low numbers of emitted oil particles $\left(N_{\mathrm{oil}} \lesssim 10^{11}\ \mathrm{m}^{-1}\right)$ independent of combustion type and (almost) independent of ambient temperature (Figure 3c) due to the relatively small Kelvin barrier. This does not hold for the kerosene case for temperatures near the Schmidt-Appleman threshold temperature (dotted blue curve in Figure 3c). However, for a larger number of emitted oil particles ($N_{\mathrm{oil}} > 10^{12}$ m^{-1}), the final freezing fraction $\phi_{\mathrm{frz,f}}$ (i.e., the

freezing fraction evaluated at the end of a simulation when ice formation is finished) decreases with increasing N_{oil}. This saturation effect arises from the larger particles of the log-normal size distribution with the lowest Kelvin barrier, which activate at an early stage and significantly deplete the water vapor, thereby preventing the smallest particles from overcoming the Kelvin barrier. This is more pronounced for a lower supersaturation forcing, that is, for kerosene combustion and/or increasing ambient temperature. Varying the geometric width has a small influence (red curves with different line styles for hydrogen case in Figure 3c). The broader the distribution, the lower is the activation fraction as a result of the increased number of particles on the left tail of the size distribution that experience a stronger Kelvin effect.

In contrast, looking at a geometric mean radius $\bar{r}_{d,oil} = 1$ nm (Figure 3d), the final freezing fraction is significantly smaller due to the strong increase of the Kelvin barrier (Figure 2). Obviously, the reduction of $\phi_{frz,f}$ at smaller particle radii is more pronounced for kerosene combustion. Moreover, the dependency on the geometric width is reversed compared to the case with $\bar{r}_{d,oil} = 15$ nm. The broader the distribution, the more oil particles are now activated because of an increased number of particles on the right tail of the size distribution that overcome the Kelvin barrier.

3.2. Competition Between Oil Particles and Soot/Ambient Aerosols

Throughout Section 3.2, volatile particle emissions are neglected ($EI_{vol} = 0$ kg^{-1}). Especially in soot-poor regimes of the kerosene combustion case, this may be a strong simplification. However, it allows us to isolate and better understand the competition between oil particles and a single other particle type (soot for kerosene and ambient aerosol for hydrogen combustion) before moving to more complex scenarios. Simulations with volatile particles included are presented in Section 3.3.

3.2.1. Final Ice Crystal Number as a Function of Oil Emission Rate

We investigate the total number of ice crystals formed as a function of $\dot{V}_{oil,eff}$. Figure 4 shows kerosene scenarios with $EI_s = 10^{15}$ kg^{-1} and hydrogen scenarios with $n_{aer} = 1{,}000$ cm^{-3} for different ambient temperatures (different panels) and oil particle sizes (line style). For low ambient temperatures (Figure 4a) and small-sized oil particles with correspondingly high N_{oil} values, $\dot{V}_{oil,eff}$ values of only a few milliliters per hour lead to a significantly higher ice crystal number than a reference kerosene case with only soot particles included. At higher $\dot{V}_{oil,eff}$, also larger assumed particles ($\bar{r}_{d,oil} = 15$ nm) are abundant in number such that the ice crystal number exceeds that of the reference kerosene case. For given $\bar{r}_{d,oil}$ and $\dot{V}_{oil,eff}$, the total ice crystal number decreases with increasing ambient temperature (Figures 4a–4c) as a consequence of the decreasing peak supersaturation and thus activation fractions. Nevertheless, for hydrogen combustion, the number of ice crystals formed on oil particles exceeds the number of ice crystals formed on ambient aerosols by up to one order of magnitude (for $\dot{V}_{oil,eff}$ of several hundred of milliliters per hour) even at high ambient temperatures (Figure 4d).

For a fixed oil emission $\dot{V}_{oil,eff}$, we observe a shift in the activation of oil particles of different radii with temperature: At low temperatures ($T_a = 215$ K) the small oil particles ($\bar{r}_{d,oil} = 1$ nm) can activate and freeze. Because of their abundance (for a fixed oil emission) the ice crystal number is substantially enhanced in both, the kerosene and the hydrogen combustion case. This trend shifts for higher temperatures ($T_a > 220$ K), where in the kerosene case the particles with $\bar{r}_{d,oil} = 5$ nm serve as efficient precursor for the highest ice crystal number at a given $\dot{V}_{oil,eff}$. This order is a combined effect of different N_{oil} values for a fixed $\dot{V}_{oil,eff}$ value (Equation 1) and the activation suppression due to the Kelvin effect. These two effects can be separated if we plot the results as a function of N_{oil} rather than $\dot{V}_{oil,eff}$ (Figure 5). Furthermore, effects such as occasionally decreasing total ice crystal numbers with increasing $\dot{V}_{oil,eff}$ for hydrogen combustion (e.g., dashed blue curve in Figure 4a) can be better understood if we examine the contributions of the individual particle types to the total ice crystal number (Figure 5).

3.2.2. Final Ice Crystal Number as a Function of Oil Particle Number

In the case of low N_{oil} values for kerosene combustion, ice crystals predominantly originate from soot particles (the solid lines in Figures 5a–5c align with the dashed lines). As the value of N_{oil} increases, the contribution of ice crystals originating from oil particles to the total ice crystal number becomes more important. Ultimately, at high

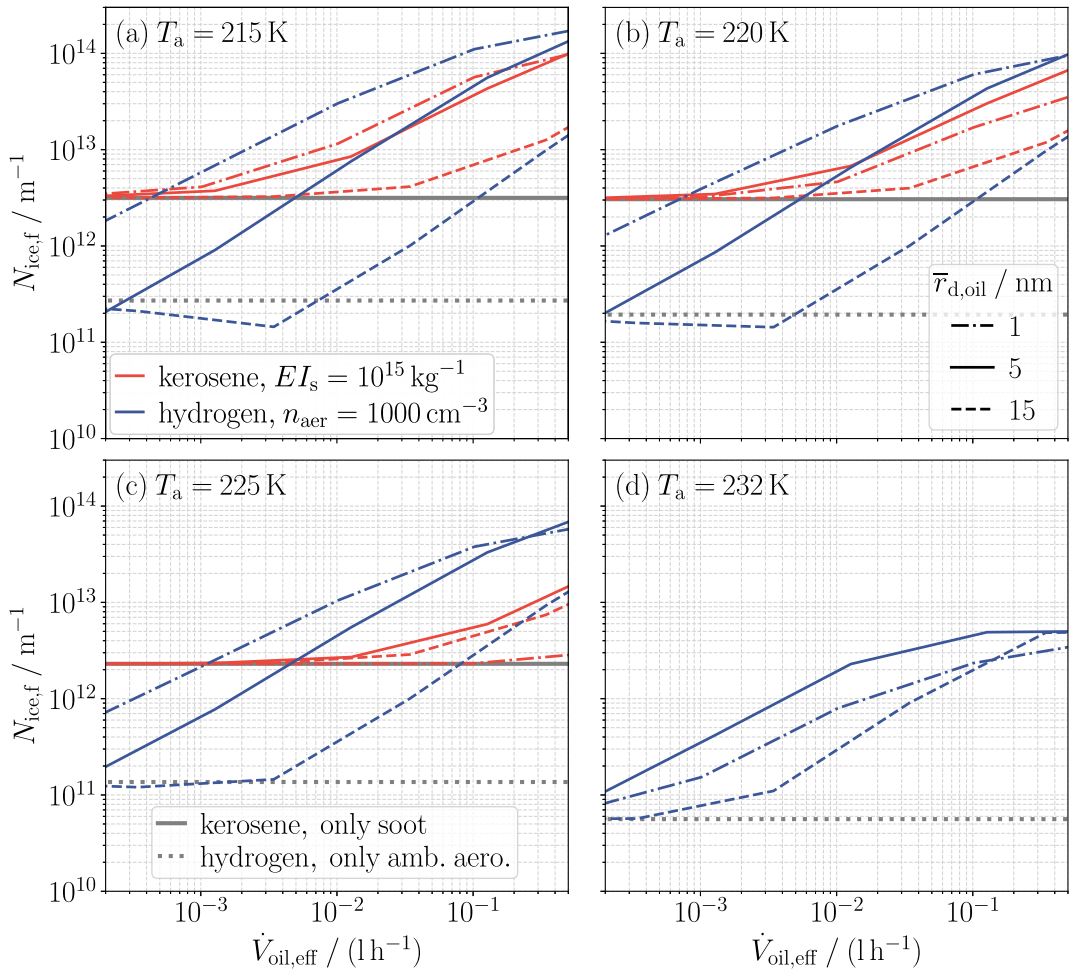

Figure 4. Total final ice crystal number $N_{ice,f}$ as a function of effective oil emission $\dot{V}_{oil,eff}$ and geometric mean radius $\bar{r}_{d,oil}$ (line style) with $\sigma_{oil} = 1.6$ for kerosene combustion with $EI_s = 10^{15}$ kg^{-1} and for hydrogen combustion with $n_{aer} = 1{,}000$ cm^{-3}. Each subplot corresponds to a different ambient temperature T_a. The solid horizontal gray lines are simulation results for kerosene combustion with only soot particles, and the dotted lines are results for hydrogen combustion with only ambient aerosols.

values of N_{oil}, oil particles become the predominant condensation nuclei (the solid lines in Figures 5a–5c start to converge toward the dotted lines). It is evident that the specific N_{oil} values at which the transition occurs are dependent upon the soot emission indices and the geometric mean radii of the oil particles. Similarly, for the hydrogen case, ice crystals predominantly originate from ambient aerosols at low N_{oil} and their formation becomes dominated by oil particles at higher N_{oil} values. This transition is contingent upon the aerosol number concentration and the geometric mean radii of the oil particles (Figures 5d–5f).

In the simulation setup of Figure 5a, soot and oil particles both feature a geometric mean radius of 15 nm. Then, the two particle types differ only in their hygroscopicity (Table 1). The activation of the oil particles is only marginally influenced by the presence of the soot particles for the high EI_s values and is essentially unaltered for the low EI_s values (the dotted lines in Figure 5a align closely with the magenta points), indicating that the different hygroscopicities play a minor role. For high N_{oil} values, we observe saturation effects (magenta points deviate from the diagonal and dashed curves bend downwards in Figure 5a). In contrast, if the initial oil particles are assumed to be smaller (in particular, $\bar{r}_{d,oil} < \bar{r}_{d,s}$), we find that the activation of the oil particles is affected by the presence of soot particles (and partly suppressed). The larger and thus earlier activated soot particles deplete the water vapor, thereby preventing the activation of some oil particles that would have activated in the absence of the soot particles (the dotted lines in Figures 5b and 5c start to deviate from the magenta points with increasing EI_s). This means, that the smaller the geometric mean radius of the oil particles the more they are hindered in their

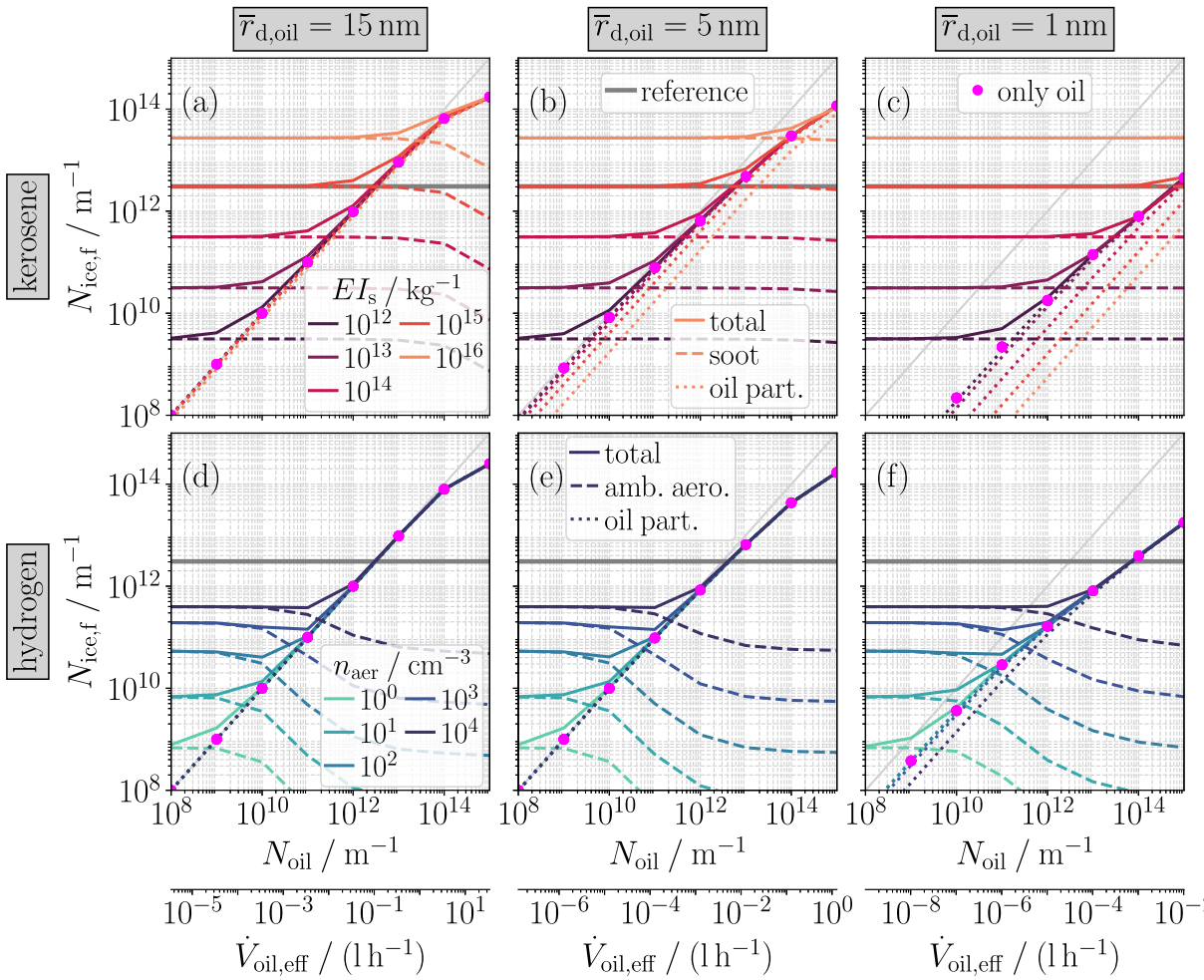

Figure 5. Final ice crystal number $N_{\mathrm{ice,f}}$ as a function of emitted oil particle number N_{oil} and geometric mean radius $\bar{r}_{\mathrm{d,oil}}$ (different columns) for kerosene combustion (first row) with different soot emission indices EI_{s} (different colors) and hydrogen combustion (second row) with different ambient aerosol number concentrations n_{aer} (different colors) for the ambient temperature $T_{\mathrm{a}} = 220$ K. Dashed and dotted line styles show the contribution of the different particle types to the total ice crystal number (solid). The magenta dots correspond to simulations including only oil particles without a second particle type. The gray horizontal lines depict a reference kerosene simulation including only soot particles with $EI_{\mathrm{s}} = 10^{15}$ kg^{-1}. The light gray diagonal line indicates a final freezing fraction $\phi_{\mathrm{frz,f}}$ of the oil particles of one. The second x-axis shows $\dot{V}_{\mathrm{oil,eff}}$ calculated with Equation 1 with $\sigma_{\mathrm{oil}} = 1.6$.

activation by two facts: First, the supersaturation encountered for the kerosene cases are not high enough to activate the smallest particles (Section 3.1; the magenta dots move downwards from Figures 5a–5c) and second, the larger soot particles reduce the supersaturation to further inhibit the activation of the smaller oil particles (the dotted lines significantly deviates from the magenta dots in Figure 5c for the higher EI_{s} values).

These two effects are less pronounced and less crucial in the hydrogen combustion scenarios where ambient aerosol particles compete with the oil particles (Figures 5d–5f). First, more oil particles can activate due to the elevated supersaturation (the magenta points are situated at higher values in Figure 5f in comparison to Figure 5c). Second, as the ambient aerosols are entrained into the plume over time, they are effectively incapable of depleting the water vapor to the extent that it can hinder the activation of the oil particles (the dotted curve only deviates notable from the magenta dots in Figure 5f for aerosol number concentrations of $n_{\mathrm{aer}} = 10{,}000$ cm^{-3}). Note, however, that the emitted oil particles partially suppress the activation of the entrained ambient aerosols for the higher N_{oil} values (down-bending dashed curves in Figures 5d–5f).

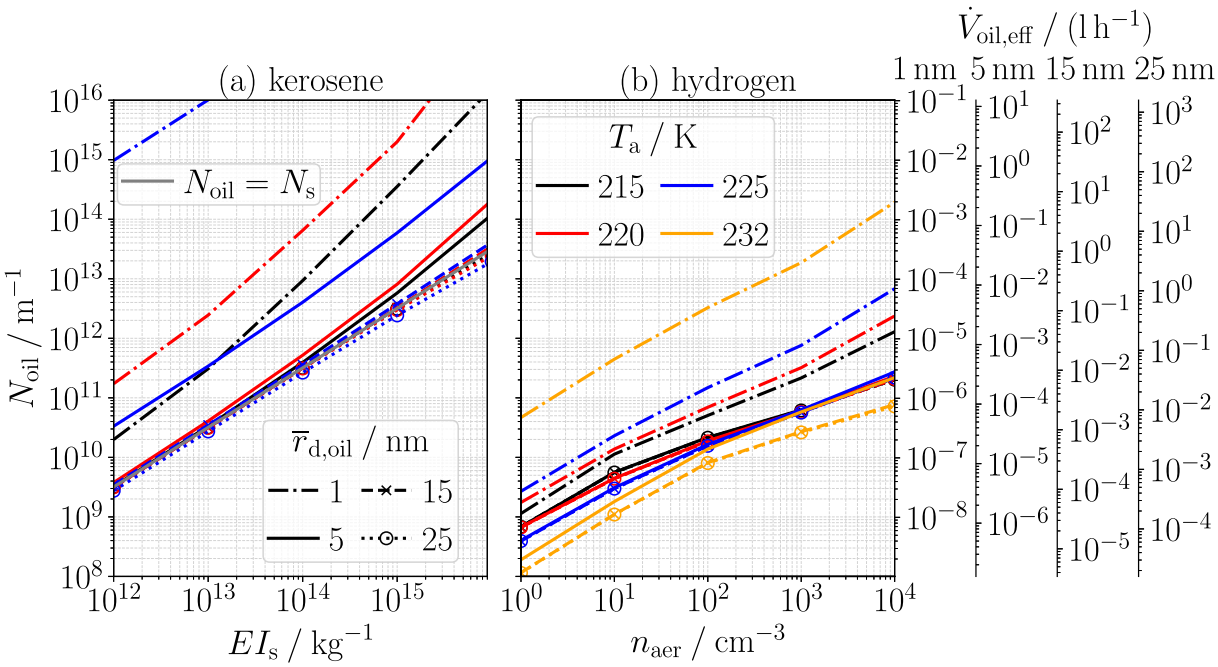

Figure 6. Transition curves where both particle types contribute equally to the number of ice crystals for (a) oil particles and soot particles for kerosene combustion and (b) oil particles and ambient aerosols for hydrogen combustion. For given temperature T_{a} (indicated by the color) and given geometric mean dry radius $\bar{r}_{\mathrm{d,oil}}$ (indicated by the line style), each line separates an oil particle and a (a) soot or (b) ambient aerosol dominated regime. The gray line in (a) indicates where the emitted oil particle number equals the number of emitted soot particles. The additional y-axes show $\dot{V}_{\mathrm{oil,eff}}$ calculated with Equation 1 for different $\bar{r}_{\mathrm{d,oil}}$ with $\sigma_{\mathrm{oil}} = 1.6$.

3.2.3. Regimes

Next, we investigate under which scenarios oil particles become the dominant condensation nuclei. For this, we determine the pairs of EI_{s} and N_{oil} values and of n_{aer} and N_{oil} values where both included particle types contribute equally to the total number of ice crystals formed. Such scenarios with equal contributions of the two involved particle types to the total ice crystal number can be evaluated in Figure 5 by determining the intersections where the dashed and dotted lines of the same colors cross. We determine these value pairs (via interpolation) for different oil particle radii $\bar{r}_{\mathrm{d,oil}}$ and ambient temperatures T_{a}. The two panels of Figure 6 display the EI_{s}–N_{oil} values for kerosene combustion and n_{aer}–N_{oil} values for hydrogen combustion, respectively. For a given combination of $\bar{r}_{\mathrm{d,oil}}$ and T_{a}, the corresponding curve in Figure 6a divides the parameter space into regimes where lubrication do or do not play a substantial role in ice crystal formation. When a specific EI_{s}–N_{oil} data point lies to the right of the corresponding curve, ice crystals form predominantly on soot particles. If the pair lies to the left, ice crystals form mainly on oil particles. In the same way we can read off from Figure 6b whether the ice crystals predominantly originate from ambient aerosols or oil particles for a given n_{aer}–N_{oil} pair.

The transition from a soot-dominated regime to an oil particle-dominated regime occurs at higher oil particle numbers when there is an increase in soot emission indices and/or a decrease in oil particle radii. For $\bar{r}_{\mathrm{d,oil}} = 15$ nm, the transition curves are nearly aligned with the line where the number of emitted oil particles is equal to the number of emitted soot particles. This confirms the weak dependency on the different hygroscopicity values. For oil particle radii that are smaller than the soot radii, the transition curves shift toward higher values of N_{oil} with increasing ambient temperatures. This is attributable to the increased Kelvin barrier of the smaller particles together with the reduction in supersaturation due to an increase in ambient temperature. In contrast, if the oil particles are assumed to be larger than the soot particles, the temperature dependency is reversed and the transition curves lie slightly below the line $N_{\mathrm{oil}} = N_{\mathrm{s}}$ for the higher EI_{s} values caused by the slightly reduced Kelvin barrier of the larger oil particles.

In the case of hydrogen combustion, the transition curves for $\bar{r}_{\mathrm{d,oil}} = 1$ nm shift to higher N_{oil} values with increasing temperature due to the high Kelvin barrier combined with the lower supersaturation at higher temperatures. This temperature dependency is reversed for the examined cases $\bar{r}_{\mathrm{d,oil}} \geq 5$ nm for $n_{\mathrm{aer}} \lesssim 1000$ cm^{-3}. This

is caused by the depletion of the water vapor by the activated emitted oil particles hindering some of the later entrained aerosols from being activated. Obviously, this depletion of water vapor by the activated oil particles has a larger influence at lower supersaturations, thus higher temperatures. Therefore, the oil particles become the dominant nuclei for already lower N_{oil}. Note that except for $T_a = 232$ K, this depends only slightly on the geometric mean radius of the oil particles. It is also noteworthy that in the case of hydrogen, in certain instances, the total number of ice crystals exhibits a slight decline with increasing N_{oil} in the vicinity of the transition region (as evidenced by the slight decline of selected solid lines in Figures 5d–5f with rising N_{oil}). This is attributed to a stronger suppression of ambient aerosol activation. However, this region is narrow, and a further increase in N_{oil} results in a higher number of ice crystals. Consequently, the oil particle-dominated region can be considered as a region where the ice crystals are present at a higher number than in the scenario with ambient aerosols only.

3.3. Competition Between Oil Particles and Other Volatile Particles

So far, we neglected the volatile particles originating from the kerosene combustion products. Especially in a soot-poor regime (here $EI_s = 10^{12}$ kg^{-1}), these particles may play an important role and compete with the oil particles for the available water vapor. If the geometric mean radii of the two volatile particle types are assumed to be the same ($\bar{r}_{d,oil} = \bar{r}_{d,vol} = 1$ nm), the critical saturation ratios for the oil particles are significantly higher than those for the well-soluble particles (Figure 2). Thus, the oil particles are partially suppressed in their activation not only due to the high Kelvin barrier but also by the presence of the other well-soluble volatile particles (the dotted lines in Figures 7a and 7b deviate from the magenta points). In contrast, the activation of the well-soluble particles is only noticeably suppressed by the oil particles when $EI_{oil} \gg EI_{vol}$ and the ambient temperature is well below the Schmidt-Appleman threshold temperature (slightly downward bending dashed curves in Figures 7a and 7b). Moreover, because of their lower critical saturation ratios, the well-soluble volatile particles still form a considerable number of ice crystals for $EI_{vol} > 10^{12}$ kg^{-1} at $T_a = 225$ K in contrast to the oil particles (Figure 7c). At this temperature and for $EI_{vol} = 10^{12}$ kg^{-1} (i.e., here the same emission index as for soot), the ice crystals formed on the well-soluble but small volatile particles are entirely masked by those formed on the larger soot particles. In fact, the soot mode becomes important already at $EI_{vol} \lesssim 10^{15}$ kg^{-1} (dashed lines are below the solid lines in Figure 7c). At lower T_a and for low EI_{oil}, the well-soluble volatile particles produce noticeable numbers of ice crystals also for $EI_{vol} = 10^{12}$ kg^{-1} (Figures 7a and 7b). However, when the total number of emitted particles is this low, the picture may be incomplete, as ambient aerosols may also contribute non-negligibly to ice crystal formation.

If the oil particles are assumed to be larger ($\bar{r}_{d,oil} = 5$ nm), the critical saturation ratios are lower than those of the well-soluble, but assumed small-sized particles ($\bar{r}_{d,vol} = 1$ nm). As a consequence, the activation of the oil particles into ice crystals is only slightly affected by the second volatile particle mode (dotted lines are close to magenta points in Figures 7d–7f). Moreover, if $EI_{oil} \gtrsim EI_{vol}$, the activation of the well-soluble volatile particles is strongly suppressed by the oil particles (down bending dashed curves in Figures 7d–7f). This results in a dominant contribution of the oil particles to the total ice crystal number at significantly lower EI_{oil} values compared to the case when both modes have the same geometric mean radius. Furthermore, the oil particles contribute considerably to the ice crystal number at $T_a = 225$ K in the case of high EI_{oil} (Figure 7f).

In summary, these illustrative simulation results show that it is a complex interplay between number, size, and solubility of different volatile particle types that determine which type dominates ice crystal formation. In these illustrative examples a rather low geometric mean radius for the well-soluble mode ($\bar{r}_{d,vol} = 1$ nm) was chosen to make the impacts of the Kelvin effect and of the solubility more discernible. Clearly in scenarios, where the well-soluble volatile particles are larger (e.g., if oil vapor mainly condenses on these particles instead of undergoing re-nucleation), their activation would be favored.

We performed analogous simulations for hydrogen combustion (Figure 8), prescribing the same number of oil particles and volatile particles as in the kerosene case (due to the lower fuel consumption in the hydrogen case, emission indices are, however, larger than in the corresponding kerosene case, see Table 1). As stated in Section 2.2, we neglect any potential differences in the properties of the volatile particles originating from hydrogen versus kerosene combustion. Moreover, we prescribe ambient aerosols with $n_{aer} = 100$ cm^{-3} instead of soot particles as a third particle type. Because of the higher supersaturations encountered in the hydrogen combustion case, activation fractions for both oil and volatile particles are consistently elevated compared to the kerosene scenario. This is particularly evident at $T_a = 225$ K, where oil particles can contribute significantly to the total ice

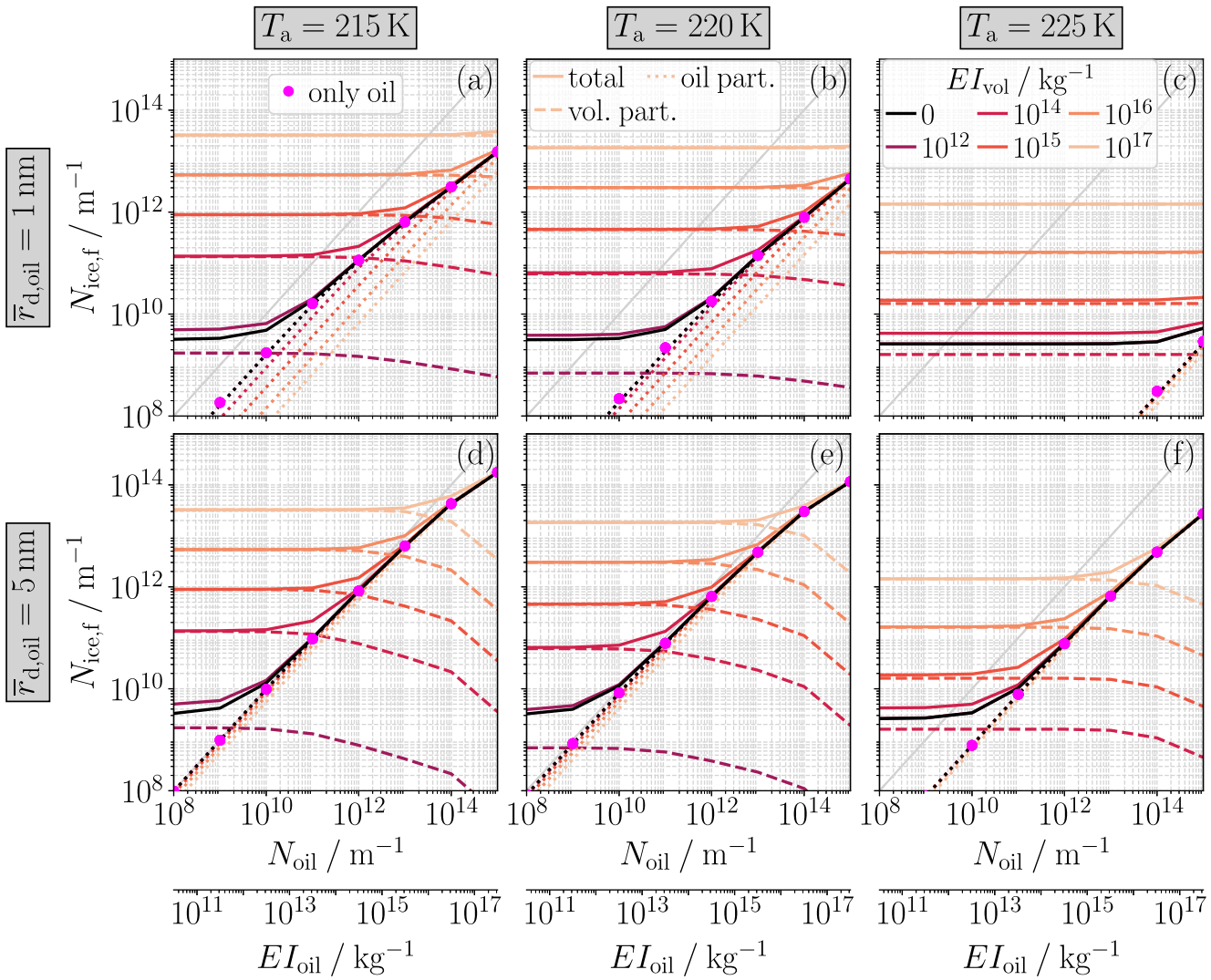

Figure 7. Final ice crystal number $N_{ice,f}$ as a function of emitted oil particle number N_{oil} (oil emission index EI_{oil}) and emission index of combustion volatile particles EI_{vol} (different colors) with $\bar{r}_{d,vol} = 1$ nm for kerosene combustion in a soot-poor regime ($EI_s = 10^{12}$ kg^{-1}). Each column corresponds to a different ambient temperature T_a and each row to a different geometric mean radius $\bar{r}_{d,oil}$. Dashed and dotted line styles show the contribution of the volatile and oil particles to the total ice crystal number (solid). The magenta dots correspond to simulations including only oil particles without other particle types. The light gray diagonal line indicates a final freezing fraction $\phi_{frz,f}$ of the oil particles of one.

crystal numbers even when their size matches that of the well-soluble volatile mode (compare Figures 7c and 8c). Moreover, for a given well-soluble volatile particle number and ambient temperature, the transition from volatile particle-dominated to oil particle-dominated ice crystal formation (intersection of dotted and dashed lines) occurs at lower N_{oil} values due to the enhanced oil particle activation under hydrogen combustion conditions. In addition, for the emission index $EI_{vol} = 2.8 \cdot 10^{12}$ kg^{-1}, the ice crystals formed on the well-soluble volatile particles are negligible (solid lines collapse with the lines for $EI_{vol} = 0$ kg^{-1} in Figures 8a–8f).

4. Discussion

The hot plume areas facilitate the production of vapors from (un-)controlled lubrication oil emissions that may nucleate to form small particles. This has yet not been measured in-flight as a chemical analysis of the composition of ultra-fine particles is challenging due to their low mass fraction. Furthermore, nanometer-sized particles are often depleted in the inlet lines of sampling systems, which enhances the uncertainty of the measurement (Dischl et al., 2024). In many investigated potential scenarios, oil particles play an important role in the formation of ice crystals. The question which of our investigated scenarios are actually representative for

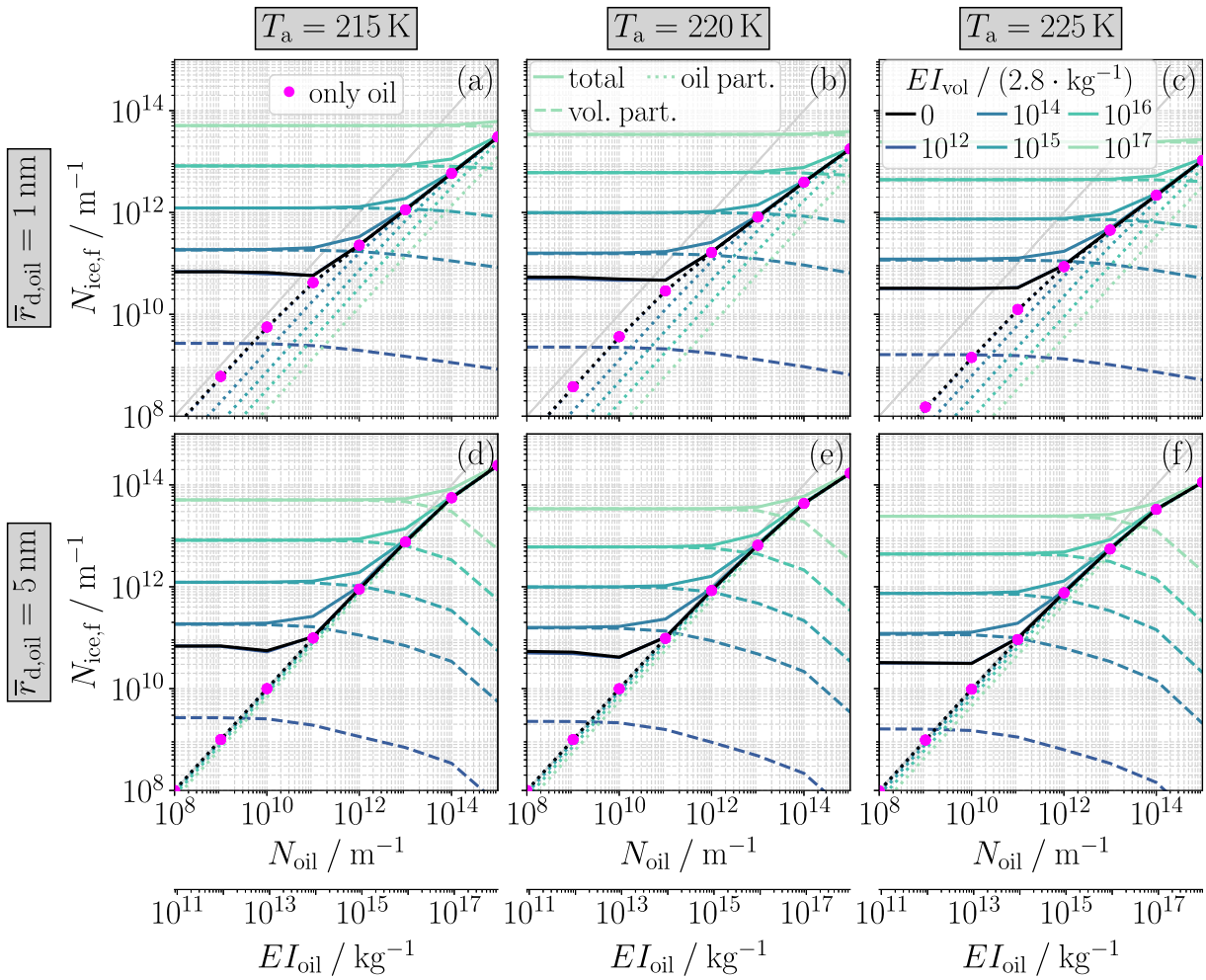

Figure 8. Final ice crystal number $N_{ice,f}$ as a function of emitted oil particle number N_{oil} (oil emission index EI_{oil}) and emission index of combustion volatile particles EI_{vol} (different colors) with $\bar{r}_{d,vol} = 1$ nm for hydrogen combustion with an ambient aerosol number concentration $n_{aer} = 100$ cm^{-3}. Each column corresponds to a different ambient temperature T_a and each row to a different geometric mean radius $\bar{r}_{d,oil}$. Dashed and dotted line styles show the contribution of the volatile and oil particles to the total ice crystal number (solid). The magenta dots correspond to simulations including only oil particles without other particle types. The light gray diagonal line indicates a final freezing fraction $\phi_{frz,f}$ of the oil particles of one.

conditions encountered during cruise can only be answered through in situ measurements that analyze the chemical and physical properties of the oil particles in relevant temperature and pressure conditions.

Past measurements for kerosene combustion for the present-day soot-rich regime ($EI_s \sim 10^{15}$ kg^{-1}) did not indicate a significant contribution of an oil particle mode to the total ice crystal number. Instead, it was experimentally shown that ice crystal formation is dominated by soot particles in the soot-rich regime (Kleine et al., 2018). A reason for this could be that oil particle numbers N_{oil} are well below the emitted soot number N_s (Figure 6a) such that the ice crystals formed on oil particles are masked by those formed on soot. Indeed, for very small oil particles $(\bar{r}_{d,oil} \sim 1$ nm$)$ the ice crystal number is still dominated by the soot emissions even if the oil particle number is two (or more) orders of magnitude higher than the soot number corresponding to $EI_s \sim 10^{15}$ kg^{-1}.

The latter result, however, might be exaggerated due to the box model approach used. Compared to large-eddy simulations, Lewellen (2020) showed that for an emitted particle type with high number emission, a box model approach has the tendency to overestimate the activation fraction due to missing mixing processes between air parcels of different ages. An overestimation in total ice crystal number by a factor of ~3 was found in Lewellen (2020) (see his Figure 2). Moreover, the small-sized ultrafine particles were found to be relatively more important in the LES simulation than in the box model approach. Although this missing mixing process may shift

the relative importance of oil particles at high soot numbers toward lower N_{oil} values, we expect that the transition to a regime dominated by oil particles will not be significantly affected in soot-poor or hydrogen scenarios. Indeed, for low number emissions or contrail formation on ambient aerosols, results of a box model approach are comparable to those of a large-eddy simulation (Lewellen, 2020). With the development of the RadMod framework (Lottermoser & Unterstrasser, 2024), a first step has been taken to account in our models for the mixing processes between air parcels in the expanding plume. Once this new dynamical framework RadMod is fully coupled with the microphysical module LCM, the present study can be refined.

The transition into an oil particle-dominated regime at significantly lower N_{oil} for lower EI_s or for hydrogen combustion (Figure 6b), does not mean that the total ice crystal numbers are necessarily higher than in a reference kerosene case with $EI_s \sim 10^{15}$ kg^{-1}. Nevertheless, due to the nonlinear dependency of the radiative forcing on the initial number of ice crystals (Burkhardt et al., 2018), the potential increase in ice crystal number caused by the oil particles may have a significant impact on the radiative forcing, even in scenarios where the ice crystal number remains lower than in a reference kerosene case.

The transition curves for the small-sized particles $\left(\bar{r}_{d,oil} \sim 1 \text{ nm}\right)$ in the soot-rich regime ($EI_s \sim 10^{15}$ kg^{-1}) occur at N_{oil} values that correspond to $\dot{V}_{oil,eff}$ values of only a few milliliters per hour-at least for temperatures well-below the Schmidt-Appleman threshold temperature (Figure 6a). Given that the oil consumption $\dot{V}_{oil}$ is typically higher (on the order of several hundred milliliters per hour (Linke-Diesinger, 2010)), together with the fact that past measurements have not indicated a significant contribution of an oil mode to the total ice crystal number in the soot-rich regime, this suggests that one (or more) of the α-values introduced in Equation 2 may be low. Assuming comparable engine configurations, switching to soot-poor regimes or hydrogen combustion is not expected to substantially alter $\alpha_{entrain}$ (provided the relative positioning of the engine core exit and the venting system remains similar) or $\alpha_{evaporate}$ (if the exit temperatures are comparable). However, the values of $\alpha_{renucleate}$ and $\alpha_{scavenging}$ might be largely increased due to the lack of soot particles as condensation sink, potentially resulting in higher N_{oil} values. In scenarios with high oil emission number $N_{oil} \gtrsim 10^{14}$ m^{-1}, the final ice crystal number for a soot-poor and low-sulfur regime (Figure 5c) or for hydrogen combustion (Figure 5f) case might be on the same order or even higher than in a reference kerosene scenario with $EI_s \sim 10^{15}$ kg^{-1}.

The potential impact of oil vapors could be reduced by designing oil breather vents that are located far away from the hot sections (e.g., off-axis) of the engine. Thus, fewer droplets penetrate the hot sections of the exhaust. In addition, oil-air separator systems used to recover oil from the mist released from the vents should be equipped with suitable filters. These filters should, ideally, remove all the oil before the air is released into the environment. Moreover, the exchange and renewal of worn seals could reduce unintentional loss. Thus, it may be beneficial to suitably adapt the maintenance cycles of the engines. Further mitigation options could be fluid bearings that do not use oil in central regions of the engine.

In the current box model version, coagulation effects are not explicitly simulated. Yet, we indirectly accounted for these effects by varying the geometric mean radius reflecting coagulation effects among the oil particles and by introducing $\alpha_{scavenging}$ accounting for the coagulation of the oil particles with other plume particles. Furthermore, we described the activation of the oil particles using the κ-Köhler theory. An alternative approach would have been to employ Frenkel, Halsey, and Hill (FHH) adsorption theory (e.g., Kumar et al., 2009; Sorjamaa & Laaksonen, 2007). This theory accounts for the attractive forces between the insoluble material and the adsorbed water molecules. These attractive forces would reduce the Kelvin barrier, enabling the activation of oil particles at lower supersaturations. However, in the limiting case of negligible small attractive forces, which we expect for hydrophobic oil particles, the FHH equilibrium saturation curve again approaches the Kelvin curve used in this study.

Focusing on oil particles and variations of their properties, we only varied the number of the other particles but kept all other properties (geometric mean and width, hygroscopicity) constant. Clearly, there would be slight quantitative differences if their actual values deviate from the prescribed ones. However, having investigated numerous scenarios of different particle numbers, the overall picture presented in this study should be largely unaffected. Moreover, F. Yu et al. (2024) suggested to use primary soot particle sizes rather than the spherical effective sizes of soot aggregates in the κ-Köhler equation. With that hypothesis, they explained the reduced soot activation observed during the ECLIF campaigns (Märkl et al., 2024; Voigt et al., 2021). This reduced soot activation would enhance the relative importance of small-sized volatile particles. Although this suggestion seems

reasonable to us, another explanation for the measured reduced soot activation could be the mixing of plume parcels of different ages (Lewellen, 2020). This process, however, is not well represented in parcel/box models (as discussed above).

For the sake of simplicity, we neglected volatile particles from combustion products in Section 3.2. Depending on their number and size, these particles may contribute significantly to the ice crystal number (Section 3.3). Nevertheless, the results in Section 3.2 demonstrate that it is not sufficient to look only at particles resulting from combustion products. If these particles from the combustion process are managed to be low in number, the presence of oil particles could still lead to high ice crystal numbers. Furthermore, we neglected ambient aerosols in the kerosene combustion case. The activation of emitted particles, however, is only marginally influenced by ambient aerosols as they gradually get mixed into the plume over time (discussed for hydrogen combustion and oil particles in Section 3.2; but it holds also for kerosene combustion and other emitted particles (not shown)) and thus the relative importance among the emitted particles will be almost unaltered. Clearly, if all emitted particle numbers are very low, the ice crystals' formation would be dominated by ambient aerosols, similar to the hydrogen case.

5. Conclusion

The rotating parts of present-day aircraft engines require a lubrication system to cool and lubricate the bearings and other parts of the engine. (Un-)controlled emissions of lubrication oil to the environment can be a source of volatile ultrafine particles when the oil is entrained into the hot exhaust plume, where it may evaporate and nucleate new particles upon cooling of the plume. Even if only a small amount of oil (a few milliliters per hour) nucleates new particles, the number of oil particles can exceed the present-day soot levels of conventional engines, assuming the newly formed particles are small (a few nanometers in size). We incorporated such oil particles as ice forming particles into the LCM box model. Many of the investigated potential scenarios showed that particles from lubrication oil may contribute significantly to ice crystal formation in soot-poor or hydrogen combustion cases. As the investigated scenarios are rather hypothetical, in situ measurements are required to assess the actual role of oil particles in the contrail ice crystal formation. If measurements will hint at a dominant role of these particles, technical adaptations of the lubrication system may be necessary to reduce their number in aircraft exhaust plumes.

Data Availability Statement

The Lagrangian Cloud Module (LCM) in a box model approach is described in detail in Bier et al. (2022, 2024). The setup and extension of the box model to simulate contrail formation on oil particles is described in Section 2.2 of the present study. The simulation results, together with the plot script required to reproduce the figures in this study, are available on a Zenodo repository (Zink, 2025).

Acknowledgments
This work has been funded by the DLR internal project H2CONTRAIL and the EU project HYDEA ("HYdrogen DEmonstrator for Aviation," https://doi.org/10.3030/101102019). We thank Klaus Gierens for an internal review of the paper draft and the reviewers for their constructive comments. Open Access funding enabled and organized by Projekt DEAL.

References

Airbus. (2020). Towards the world's first hydrogen-powered commercial aircraft. Retrieved from https://www.airbus.com/en/innovation/energy-transition/hydrogen/zeroe#concepts

Bier, A., & Burkhardt, U. (2022). Impact of parametrizing microphysical processes in the jet and vortex phase on contrail cirrus properties and radiative forcing. *Journal of Geophysical Research*, *127*(23), e2022JD036677. https://doi.org/10.1029/2022JD036677

Bier, A., Unterstrasser, S., & Vancassel, X. (2022). Box model trajectory studies of contrail formation using a particle-based cloud microphysics scheme. *Atmospheric Chemistry and Physics*, *22*(2), 823–845. https://doi.org/10.5194/acp-22-823-2022

Bier, A., Unterstrasser, S., Zink, J., Hillenbrand, D., Jurkat-Witschas, T., & Lottermoser, A. (2024). Contrail formation on ambient aerosol particles for aircraft with hydrogen combustion: A box model trajectory study. *Atmospheric Chemistry and Physics*, *24*(4), 2319–2344. https://doi.org/10.5194/acp-24-2319-2024

Bräuer, T., Voigt, C., Sauer, D., Kaufmann, S., Hahn, V., Scheibe, M., et al. (2021). Reduced ice number concentrations in contrails from low-aromatic biofuel blends. *Atmospheric Chemistry and Physics*, *21*(22), 16817–16826. https://doi.org/10.5194/acp-21-16817-2021

Brock, C. A., Froyd, K. D., Dollner, M., Williamson, C. J., Schill, G., Murphy, D. M., et al. (2021). Ambient aerosol properties in the remote atmosphere from global-scale in situ measurements. *Atmospheric Chemistry and Physics*, *21*(4), 15023–15063. https://doi.org/10.5194/acp-21-15023-2021

Burkhardt, U., Bock, L., & Bier, A. (2018). Mitigating the contrail cirrus climate impact by reducing aircraft soot number emissions. *npj Climate and Atmospheric Science*, *1*(1), 37. https://doi.org/10.1038/s41612-018-0046-4

Decker, Z. C. J., Alpert, P. A., Ammann, M., Anet, J. G., Bauer, M., Cui, T., et al. (2024). Emission and Formation of Aircraft Engine Oil Ultrafine Particles. *ACS ES&T Air*, *1*(12), 1662–1672. https://doi.org/10.1021/acsestair.4c00184

Dischl, R., Sauer, D., Voigt, C., Harlaß, T., Sakellariou, F., Märkl, R., et al. (2024). Measurements of particle emissions of an A350-941 burning 100% sustainable aviation fuels in cruise. *Atmospheric Chemistry and Physics*, *24*(19), 11255–11273. https://doi.org/10.5194/acp-24-11255-2024

Fushimi, A., Saitoh, K., Fujitani, Y., & Takegawa, N. (2019). Identification of jet lubrication oil as a major component of aircraft exhaust nanoparticles. *Atmospheric Chemistry and Physics*, *19*(9), 6389–6399. https://doi.org/10.5194/acp-19-6389-2019

Grewe, V., Bock, L., Burkhardt, U., Dahlmann, K., Gierens, K., Hüttenhofer, L., et al. (2017). Assessing the climate impact of the AHEAD multi-fuel blended wing body. *Meteorologische Zeitschrift*, *26*(6), 711–725. https://doi.org/10.1127/metz/2016/0758

Haverkamp, H., Wilhelm, S., Sorokin, A., & Arnold, F. (2004). Positive and negative ion measurements in jet aircraft engine exhaust: Concentrations, sizes and implications for aerosol formation. *Atmospheric Environment*, *38*(18), 2879–2884. https://doi.org/10.1016/j.atmosenv.2004.02.028

Kaiser, C., Hendricks, J., Righi, M., Jöckel, P., Tost, H., Kandler, K., et al. (2019). Global aerosol modeling with MADE3 (v3.0) in EMAC (based on v2.53): Model description and evaluation. *Geoscientific Model Development*, *12*(1), 541–579. https://doi.org/10.5194/gmd-12-541-2019

Kärcher, B. (2018). Formation and radiative forcing of contrail cirrus. *Nature Communications*, *9*(1), 1824. https://doi.org/10.1038/s41467-018-04068-0

Kärcher, B., Burkhardt, U., Bier, A., Bock, L., & Ford, I. J. (2015). The microphysical pathway to contrail formation. *Journal of Geophysical Research*, *120*(15), 7893–7927. https://doi.org/10.1002/2015JD023491

Kärcher, B., & Yu, F. (2009). Role of aircraft soot emissions in contrail formation. *Geophysical Research Letters*, *36*(1), L01804. https://doi.org/10.1029/2008GL036649

Kleine, J., Voigt, C., Sauer, D., Schlager, H., Scheibe, M., Jurkat-Witschas, T., et al. (2018). In situ observations of ice particle losses in a young persistent contrail. *Geophysical Research Letters*, *45*(24), 13553–13561. https://doi.org/10.1029/2018GL079390

Kumar, B., Sokolik, I. N., & Nenes, A. (2009). Parameterization of cloud droplet formation for global and regional models: Including adsorption activation from insoluble CCN. *Atmospheric Chemistry and Physics*, *9*(7), 2517–2532. https://doi.org/10.5194/acp-9-2517-2009

Lee, D. S., Fahey, D. W., Skowron, A., Allen, M. R., Burkhardt, U., Chen, Q., et al. (2021). The contribution of global aviation to anthropogenic climate forcing for 2000 to 2018. *Atmospheric Environment*, *244*, 117834. https://doi.org/10.1016/j.atmosenv.2020.117834

Lewellen, D. C. (2020). A large-eddy simulation study of contrail ice number formation. *Journal of the Atmospheric Sciences*, *77*(7), 2585–2604. https://doi.org/10.1175/JAS-D-19-0322.1

Linke-Diesinger, A. (2010). *Systems of Commercial Turbofan Engines: An Introduction to Systems Functions*. Springer.

Lottermoser, A., & Unterstrasser, S. (2024). Towards intermediate complexity modelling of contrail formation: The new dynamical framework RadMod. *Aeronautical Journal*, *129*(1332), 1–29. https://doi.org/10.1017/aer.2024.130

Märkl, R. S., Voigt, C., Sauer, D., Dischl, R. K., Kaufmann, S., Harlaß, T., et al. (2024). Powering aircraft with 100% sustainable aviation fuel reduces ice crystals in contrails. *Atmospheric Chemistry and Physics*, *24*(6), 3813–3837. https://doi.org/10.5194/acp-24-3813-2024

Minikin, A., Petzold, A., Ström, J., Krejci, R., Seifert, M., van Velthoven, P., et al. (2003). Aircraft observations of the upper tropospheric fine particle aerosol in the northern and southern hemispheres at midlatitudes. *Geophysical Research Letters*, *30*(10), 1503. https://doi.org/10.1029/2002GL016458

Moore, R. H., Thornhill, K. L., Weinzierl, B., Sauer, D., D'Ascoli, E., Kim, J., et al. (2017). Biofuel blending reduces particle emissions from aircraft engines at cruise conditions. *Nature*, *543*(7645), 411–415. https://doi.org/10.1038/nature21420

Petters, M. D., & Kreidenweis, S. M. (2007). A single parameter representation of hygroscopic growth and cloud condensation nucleus activity. *Atmospheric Chemistry and Physics*, *7*(8), 1961–1971. https://doi.org/10.5194/acp-7-1961-2007

Ponsonby, J., King, L., Murray, B. J., & Stettler, M. E. J. (2024). Jet aircraft lubrication oil droplets as contrail ice-forming particles. *Atmospheric Chemistry and Physics*, *24*(3), 2045–2058. https://doi.org/10.5194/acp-24-2045-2024

Quante, G., Voß, S., Bullerdiek, N., Voigt, C., & Kaltschmitt, M. (2024). Hydroprocessing of fossil fuel-based aviation kerosene – Technology options and climate impact mitigation potentials. *Atmospheric Environment X*, *22*, 100259. https://doi.org/10.1016/j.aeaoa.2024.100259

Richardson, E. S. (2025). Contrail Formation Criterion for Assessment of Alternative Propulsion Technologies. *Journal of Propulsion and Power*, *41*(3), 1–13. https://doi.org/10.2514/1.b39430

Riechers, B., Wittbracht, F., Hütten, A., & Koop, T. (2013). The homogeneous ice nucleation rate of water droplets produced in a microfluidic device and the role of temperature uncertainty. *Physical Chemistry Chemical Physics*, *15*(16), 5873–5887. https://doi.org/10.1039/c3cp42437e

Schumann, U. (1996). On conditions for contrail formation from aircraft exhausts. *Meteorologische Zeitschrift*, *5*(1), 4–23. https://doi.org/10.1127/metz/5/1996/4

Sölch, I., & Kärcher, B. (2010). A large-eddy model for cirrus clouds with explicit aerosol and ice microphysics and Lagrangian ice particle tracking. *Quarterly Journal of the Royal Meteorological Society*, *136*(653), 2074–2093. https://doi.org/10.1002/qj.689

Sorjamaa, R., & Laaksonen, A. (2007). The effect of H_2O adsorption on cloud drop activation of insoluble particles: A theoretical framework. *Atmospheric Chemistry and Physics*, *7*(24), 6175–6180. https://doi.org/10.5194/acp-7-6175-2007

Ungeheuer, F., Caudillo, L., Ditas, F., Simon, M., van Pinxteren, D., Kilic, D., et al. (2022). Nucleation of jet engine oil vapours is a large source of aviation-related ultrafine particles. *Communications Earth & Environment*, *3*(319), 1–8. https://doi.org/10.1038/s43247-022-00653-w

Ungeheuer, F., van Pinxteren, D., & Vogel, A. L. (2021). Identification and source attribution of organic compounds in ultrafine particles near frankfurt international airport. *Atmospheric Chemistry and Physics*, *21*(5), 3763–3775. https://doi.org/10.5194/acp-21-3763-2021

Unterstrasser, S., & Gierens, K. (2010). Numerical simulations of contrail-to-cirrus transition - Part 2: Impact of initial ice crystal number, radiation, stratification, secondary nucleation and layer depth. *Atmospheric Chemistry and Physics*, *10*(4), 2037–2051. https://doi.org/10.5194/acp-10-2037-2010

Unterstrasser, S., & Sölch, I. (2014). Optimisation of simulation particle number in a Lagrangian ice microphysical model. *Geoscientific Model Development*, *7*, 695–709. https://doi.org/10.5194/gmd-7-695-2014

Vancassel, X., Mirabel, P., & Garnier, F. (2014). Numerical simulation of aerosols in an aircraft wake using a 3D LES solver and a detailed microphysical model. *International Journal of Sustainable Aviation*, *1*(2), 139–159. https://doi.org/10.1504/IJSA.2014.065480

Voigt, C., Kleine, J., Sauer, D., Moore, R. H., Bräuer, T., Le Clercq, P., et al. (2021). Cleaner burning aviation fuels can reduce contrail cloudiness. *Communications Earth & Environment*, *2*(1), 114. https://doi.org/10.1038/s43247-021-00174-y

Yu, F., Kärcher, B., & Anderson, B. E. (2024). Revisiting contrail ice formation: Impact of primary soot particle sizes and contribution of volatile particles. *Environmental Science & Technology*, *58*(40), 17650–17660. https://doi.org/10.1021/acs.est.4c04340

Yu, F., & Turco, R. P. (1997). The role of ions in the formation and evolution of particles in aircraft plumes. *Geophysical Research Letters*, *24*(15), 1927–1930. https://doi.org/10.1029/97gl01822

Yu, Z., Liscinsky, D. S., Winstead, E. L., True, B. S., Timko, M. T., Bhargava, A., et al. (2010). Characterization of lubrication oil emissions from aircraft engines. *Environmental Science & Technology*, *44*(24), 9530–9534. https://doi.org/10.1021/es102145z

Yu, Z., Timko, M. T., Herndon, S. C., Richard, C. M.-L., Beyersdorf, A. J., Ziemba, L. D., et al. (2019). Mode-specific, semi-volatile chemical composition of particulate matter emissions from a commercial gas turbine aircraft engine. *Atmospheric Environment*, *218*, 116974. https://doi.org/10.1016/j.atmosenv.2019.116974

Zink, J. (2025). Box model simulation results and plotting script for oil particle study [Dataset]. *Zenodo*. https://doi.org/10.5281/zenodo.14717632